Spectroscopic Investigation of Peridinin Analogues Having Different π-Electron Conjugated Chain Lengths: Exploring the Nature of the Intramolecular Charge Transfer State

Dariusz M. Niedzwiedzki,[†] Nirmalya Chatterjee,[†] Miriam M. Enriquez,[†] Takayuki Kajikawa,[‡] Shinji Hasegawa,[‡] Shigeo Katsumura,[‡] and Harry A. Frank*[,†]

Department of Chemistry, University of Connecticut, U-3060, 55 North Eagleville Road, Storrs, Connecticut 06269-3060, Department of Chemistry, Kwansei Gakuin University, 669-1337, Hyogo, Japan

Received: April 28, 2009; Revised Manuscript Received: August 28, 2009

The lifetime of the lowest excited singlet (S_1) state of peridinin and many other carbonyl-containing carotenoids and polyenes has been reported to depend on the polarity of the solvent. This effect has been attributed to the presence of an intramolecular charge transfer (ICT) state in the manifold of excited states for these molecules. The nature of this ICT state has yet to be elucidated. In the present work, steady-state and ultrafast time-resolved optical spectroscopy have been performed on peridinin and three synthetic analogues, C_{33}-peridinin, C_{35}-peridinin, and C_{39}-peridinin, which have different numbers of conjugated carbon−carbon double bonds. Otherwise, the molecules are structurally similar in that they possess the same functional groups. The trends in the positions of the steady-state and transient spectral profiles for this systematic series of molecules allow an assignment of the spectral features to transitions involving the S_0, S_1, S_2, and ICT states. A kinetics analysis reveals the lifetimes of the excited states and the dynamics of their excited state deactivation pathways. The most striking observation in the data is that the lifetime of the ICT state converges to the same value of 10.0 ± 2.0 ps in the polar solvent, methanol, for all the peridinin analogues, regardless of the extent of π-electron conjugation. This suggests that the ICT state is highly localized on the lactone ring, which is a common structural feature in all the molecules. The data further suggest that the S_1 and ICT states behave independently and that the ICT state is populated from both S_1 and S_2, the rate and efficiency from S_1 being dependent on the length of the π-electron chain of the carotenoid and the solvent polarity.

Introduction

For polyenes and carotenoids, transitions to and from the ground state, S_0, to the lowest-lying excited state, S_1, are both symmetry- and parity-forbidden.[1−5] The forbiddenness of the $S_0 \leftrightarrow S_1$ transitions has been explained theoretically by a model assigning A_g^- symmetry to both states and supported experimentally by the lack of a solvent effect on both the (weak) $S_1 \rightarrow S_0$ fluorescence spectrum and the S_1 lifetime.[6−8] However, for polyenes and carotenoids possessing a carbonyl functional group, a profound effect of solvent polarity on the lifetime of the lowest excited singlet state has been reported to be as large as 1 or 2 orders of magnitude for some carotenoids and apocarotenal molecules.[9−15] It has been proposed that these findings are consistent with the presence of an intramolecular charge transfer (ICT) state due to the presence of the carbonyl group in conjugation with the π-electron system of double bonds.[8−10] It has been argued that changes in the position of the ICT state relative to the S_1 state rationalize the dependence on solvent polarity of the S_1 lifetime.[8,10] However, the precise nature of the ICT state has yet to be elucidated. Experiments on carbonyl-containing carotenoids having different extents of π-electron conjugation have shown that the effect of the solvent becomes more pronounced with a decreasing number of carbon−carbon double bonds, N.[12,13,15] Thus, whatever perturbation is responsible for the solvent effect, it becomes more pronounced as the conjugated system of π-electron double bonds is shortened. Proposals for the nature of the ICT state include its being a separate electronic state from S_1,[9,16−19] quantum mechanically mixed with S_1,[20,21] or simply S_1 itself but possessing a large intrinsic dipole moment due to coupling with S_2.[22]

To explore the nature of the ICT state in carbonyl-containing carotenoids, we synthesized a series of peridinin analogues having different numbers of conjugated carbon−carbon double bonds (Figure 1). Naturally occurring peridinin has a C_{37} carbon skeleton and $N = 8$ with a carbonyl group in the conjugated system. The synthetic analogues are C_{33}-peridinin, which has two fewer double bonds than peridinin; C_{35}-peridinin, which has one fewer double bond than peridinin; and C_{39}-peridinin, which has one more double bond than peridinin. In all other ways, these molecules are structurally similar to peridinin (Figure 1) in that they possess the same functional groups. The trends in the spectroscopic and kinetic properties exhibited by this systematic series of peridinin analogues are consistent with a model in which the ICT state behaves independently from S_1 and accepts population from S_1 at a rate that depends on both the length of the conjugated π-electron chain and the polarity of the solvent.

Experimental Methods

Peridinin was extracted from *Amphidinium carterae* cells as previously described.[23,24] The synthesis of the C_{33}-, C_{35}-, and C_{39}-peridinin analogues will be described elsewhere. The analogues were supplied as dried samples. Prior to the spectroscopic experiments, all molecules were purified using a Millipore Waters 600E high-performance liquid chromatograph (HPLC) employing a YMC-Carotenoid C_{30} column and a Waters

* To whom correspondence should be addressed. Fax: 860-486-6558. E-mail: harry.frank@uconn.edu.
[†] University of Connecticut.
[‡] Kwansei Gakuin University.

10.1021/jp903923r CCC: $40.75
Published on Web 09/23/2009

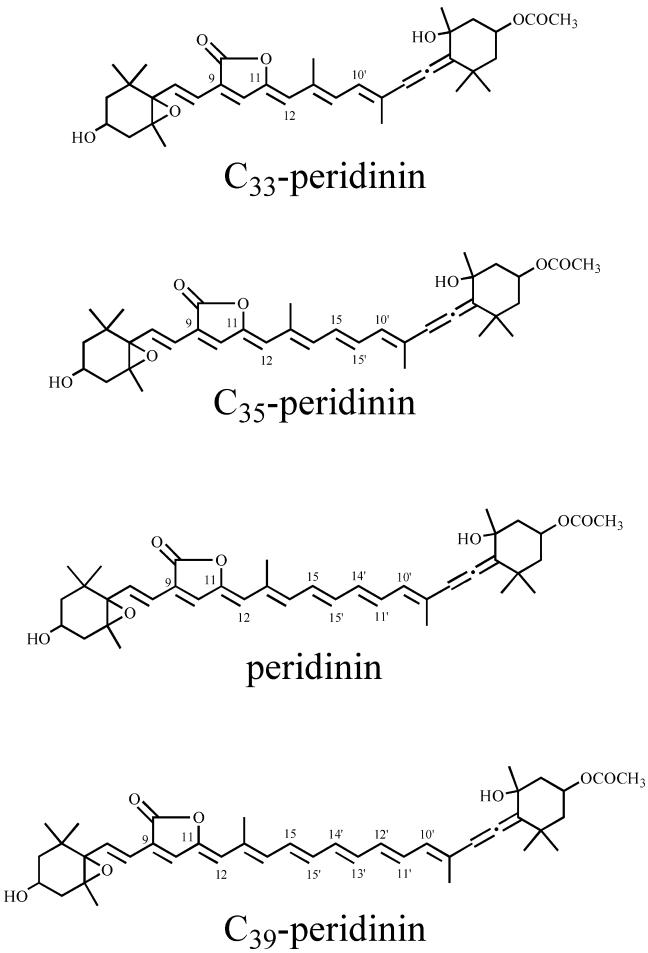

Figure 1. Structures of peridinin and synthetic C_{33}-, C_{35}- and C_{39}-peridinin analogues.

996 single diode-array detector. The isocratic mobile phase consisted of 87/10/3 v/v/v acetonitrile/methanol/water at a flow rate of 0.8 mL/min. HPLC peaks corresponding to the all-trans molecules were collected, dried under a gentle stream of gaseous nitrogen, and stored at −80 °C until used in the spectroscopic experiments. The molecules were dissolved in solvents with increasing polarity, $P(\varepsilon)$, but with similar polarizability, $P(n)$: *n*-hexane ($P(\varepsilon) = 0.229$, $P(n) = 0.228$, Fisher Scientific), methyl *tert*-butyl ether (MTBE, $P(\varepsilon) = 0.526$, $P(n) = 0.226$, Fisher Scientific), ethyl acetate ($P(\varepsilon) = 0.626$, $P(n)$=0.226, Aldrich Chemicals), 2-propanol ($P(\varepsilon) = 0.852$, $P(n) = 0.230$, Fisher Scientific), and methanol ($P(\varepsilon) = 0.913$, $P(n) = 0.203$, Aldrich Chemicals).

Steady-state absorption spectra were recorded using a Varian Cary 50 UV−visible spectrophotometer. Steady-state fluorescence measurements were performed using a Jobin-Yvon Horiba Fluorolog-3 equipped with a Hamamatsu R928P detector and a 450 W ozone-free Osram XBO xenon arc lamp. The fluorescence was monitored at a right angle relative to the excitation. Excitation and emission monochromator slits were set to a bandpass of 5 nm. All fluorescence spectra were corrected for the instrument response profiles using correction factors generated using a standard lamp.

Transient pump−probe absorption experiments were carried out using a femtosecond transient absorption spectrometer system previously described.[25] Briefly, the system is based on an amplified, 1 kHz Ti:Sapphire laser (Spectra-Physics). Pump pulses with a duration of ∼60 fs were obtained from an OPA-800C optical parametric amplifier (Spectra-Physics). Probe laser pulses were derived from a white light continuum (450−800 nm in the visible region and 800−1450 nm in the NIR) generated by a 3 mm sapphire plate (Ultrafast Systems LLC). For detection in the visible spectral range, a charge-coupled detector S2000 with a 2048 pixel array from Ocean Optics was used. In the NIR region, a 512 pixel array SU-LDV high-resolution InGaAs digital line camera from Sensors Unlimited was used. The pump and probe beams were overlapped at the sample at the magic-angle (54.7°) polarization. The signals were averaged over 5 s. The samples were pumped as close as possible into the 0−0 vibronic band of the $S_0 \rightarrow S_2$ steady-state absorption spectrum. The pump wavelengths are listed in Table 1. The energy of the pump beam was set to 1 μJ/pulse in a spot size of 1 mm diameter, corresponding to an intensity between 3.0 and 3.3 $\times$ 10^{14} photons/cm^2/pulse. The full width at half-maximum of the cross correlation in methanol for excitation pulses at 485 nm and probe pulses at 565 nm was determined to be ∼170 fs, according to the procedure of Ziolek et al.,[26] and was assumed to be the same for other solvents due to the similarity of refractive indices. The pump wavelengths were 470 nm for C_{33}- and C_{35}-peridinin, 485 nm for peridinin, and 501 nm for C_{39}-peridinin. The samples were adjusted to an optical density of 1.5−2.5 at the excitation wavelength in a 1 cm cuvette and were then transferred to a 2 mm path length cuvette in the spectrometer, where they were mixed continuously using a magnetic microstirrer to prevent photodegradation. The integrity of the samples was checked by taking steady-state absorption spectra before and after every experiment. Chirp correction of the transient absorption spectra was performed using Surface Explorer (v.1.0.6) software (Ultrafast Systems LCC) by building a dispersion correction curve from a set of initial times of transient signals obtained from single wavelength fits of representative kinetics from a pure solvent sample. The number of principal kinetic components was determined by singular value decomposition. Transient absorption kinetics were analyzed at specific wavelengths by fitting the temporal profiles to a sum of exponentials equation incorporating a Gaussian instrumental response function using Surface Explorer software.

Fluorescence lifetime measurements were performed using a time-correlated, single photon counting (TCSPC) module installed on a Jobin-Yvon Horiba Fluorolog 3 spectrometer. The system consisted of a single photon counting controller FluoroHub 2.0 (J-Y Horiba), a Hamamatsu R928P detector, and a pulsed NanoLed-470 L diode as the excitation light source that provided 466 nm excitation having a pulse duration of <200 ps. The fluorescence was monitored at 490 nm for C_{33}-peridinin and at 550 nm for C_{35}-peridinin. Fitting of the fluorescence kinetics was carried out using Data Analysis Software DAS version 6.4 (JY Horiba).

Results

Steady-State Absorption. Steady-state absorption spectra of peridinin and C_{33}-, C_{35}-, and C_{39}-peridinin analogues in *n*-hexane, MTBE, ethyl acetate, 2-propanol, and methanol are shown in Figure 2. In all solvents, the spectra shift systematically by ∼20 nm to longer wavelength with increasing π-electron conjugation chain length. In the nonpolar solvent, *n*-hexane (Figure 2A), the absorption spectral line shapes of all the molecules exhibit resolved vibronic bands. The vibronic features become less pronounced with increasing solvent polarity (Figure 2B−D). The vibronic bands are absent from the absorption spectra taken in the highly polar solvent, methanol (Figure 2E), resulting in broad unstructured line shapes for all the molecules

TABLE 1: Dynamics of the S_1 and ICT States of C_{33}-Peridinin, C_{35}-Peridinin, Peridinin and C_{39}-Peridinin Determined by Fitting the Rise and Decay Kinetics of the Transient Absorption Signals Corresponding to the $S_1 \rightarrow S_n$ and ICT $\rightarrow S_n$ Transitions[a]

			lifetime			
molecule	solvent	probe λ/nm	τ_1/fs	τ_2/ps	τ_3/ps	τ_4/ps[b]
C_{33}-peridinin	*n*-hexane	606	220 ± 60	4 ± 2	130 ± 40	4200[c] ± 200
	MTBE	572	<170	3.3 ± 1.0	62 ± 8	200 ± 30
	ethyl acetate	548	<170	1.5 ± 0.2	10 ± 1	37 ± 3
	2-propanol	546	<170	13 ± 3	40 ± 5	−
	methanol	513	190 ± 50	4 ± 1	10 ± 2	−
C_{35}-peridinin	*n*-hexane	489	210 ± 50	70 ± 30	1000[c] ± 100	−
		639	210 ± 50	45 ± 20	1000[c] ± 100	−
	MTBE	530	210 ± 50	22 ± 5	350 ± 20	−
		610	210 ± 50	7.7 ± 1.0	450 ± 20	−
	ethyl acetate	526	<170	2.1 ± 0.5	92 ± 6	−
		592	<170	1.8 ± 0.2	81 ± 3	−
	2-propanol	524	<170	5 ± 1	58 ± 3	−
		586	<170	2.5 ± 0.7	43 ± 3	−
	methanol	507	<170	2.6 ± 0.7	12 ± 2	−
		555	<170	1.2 ± 0.3	9.2 ± 0.5	−
peridinin	*n*-hexane	516	<170	1.4 ± 0.6	186 ± 6	−
		657	<170	8 ± 2	186 ± 10	−
	MTBE	521	<170	5 ± 1	185 ± 10	−
		649	<170	4 ± 1	180 ± 10	−
	ethyl acetate	530	<170	3.0 ± 0.3	88 ± 2	−
		638	<170	3.6 ± 0.3	88 ± 2	−
	2-propanol	546	<170	5 ± 1	54 ± 3	−
		628	<170	2.1 ± 0.4	46 ± 1	−
	methanol	545	<170	1.5 ± 0.3	11 ± 1	−
		592	<170	1.2 ± 0.1	9 ± 1	−
C_{39}-peridinin	*n*-hexane	536	200 ± 50	1.7 ± 0.5	41 ± 2	−
	MTBE	540	<170	1.3 ± 0.8	41 ± 2	−
	ethyl acetate	539	<170	1.0 ± 1.0	41 ± 2	−
		676	<170	2.3 ± 0.5	41 ± 2	−
	2-propanol	542	<170	0.8 ± 0.3	33 ± 1	−
		674	<170	1.3 ± 0.4	29 ± 1	−
	methanol	543	<170	0.8 ± 0.4	12 ± 1	−
		664	<170	0.5 ± 0.3	9 ± 1	−

[a] The uncertainties in the numbers were determined from an examination of the region of solution for each fitted parameter based on the values of the residuals. [b] Dash means that an additional component was not necessary for a good fit. [c] Values obtained from TCSPC.

except C_{33}-peridinin (thin solid line in Figure 2E), where small inflections attributable to residual vibronic bands are evident.

Steady-State Fluorescence. Fluorescence spectra of peridinin and C_{33}-, C_{35}-, and C_{39}-peridinin analogues are shown in Figure 3. For peridinin and the C_{33}- and C_{35}-peridinin analogues, the spectra are broad and substantially red-shifted relative to their respective absorption spectra. This indicates that the emission originates primarily from the S_1 state rather than the S_2 state for the molecules dissolved in nonpolar solvents. The assignment of the emission as S_1-like is supported by the fact that the maxima in the spectral traces do not shift substantially when the molecules are dissolved in the highly polarizable solvent, carbon disulfide ($P(n) = 0.357$), as compared with their position in *n*-hexane ($P(n) = 0.229$) (see Figure S1). This is also consistent with the idea that the $S_0 \rightarrow S_1$ transition has a negligible dipole moment and, consequently, experiences only very small interactions with the solvent environment. Vibronic features in the S_1 fluorescence spectra are most evident for the molecules dissolved in the nonpolar solvent, *n*-hexane (Figure 3A). These features become better resolved as the π-electron conjugation chain length is increased. For example, compare C_{33}-peridinin in MTBE (thin solid line in Figure 3B) with C_{39}-peridinin in the same solvent (dotted line in Figure 3B). In general, the vibronic features diminish with increasing solvent polarity, and additional fluorescence intensity appears at longer wavelength. This additional fluorescence is most noticeable for the molecules dissolved in methanol and is attributable to emission from the ICT state that becomes evident as it is stabilized below S_1 (see below).

C_{39}-peridinin is unique in the series in that its fluorescence spectrum in the visible region (dotted lines in Figure 3) contains emission originating from both the S_1 and S_2 states. In *n*-hexane, emission from the S_2 state is more intense than emission from S_1 (dotted line in Figure 3A). In the more polar solvents, the S_1-like emission dominates.

Transient Absorption. Transient absorption spectra of peridinin and C_{33}-, C_{35}-, and C_{39}-peridinin analogues taken in different solvents at various delay times after excitation into the S_2 state are shown in Figure 4. Excitation of the shortest molecule in the series, C_{33}-peridinin (Figure 4A−E), results in a rapid (~200 fs) build-up of excited-state absorption (ESA) in the wavelength range 500−700 nm. The transient absorption spectra taken at the earliest times are broad and asymmetric in all solvents and shift from longer to shorter wavelength within a few hundred femtoseconds. This behavior is exemplified in the spectra of C_{33}-peridinin in ethyl acetate (Figure 4C), where the 0 ps ESA band exhibits a broad asymmetric line shape that narrows within 200 ps. In addition, the 0 ps time spectrum of C_{33}-peridinin in ethyl acetate (Figure 4C) shows a slight dip in the spectrum at ~600 nm. The dip and narrowing are noticeable in all the early time traces for C_{33}-peridinin in all solvents. Upon closer examination, it can be seen that the narrowing is caused by the signal on the long wavelength side of the dip decaying in a few hundred femtoseconds, whereas the signal on the short

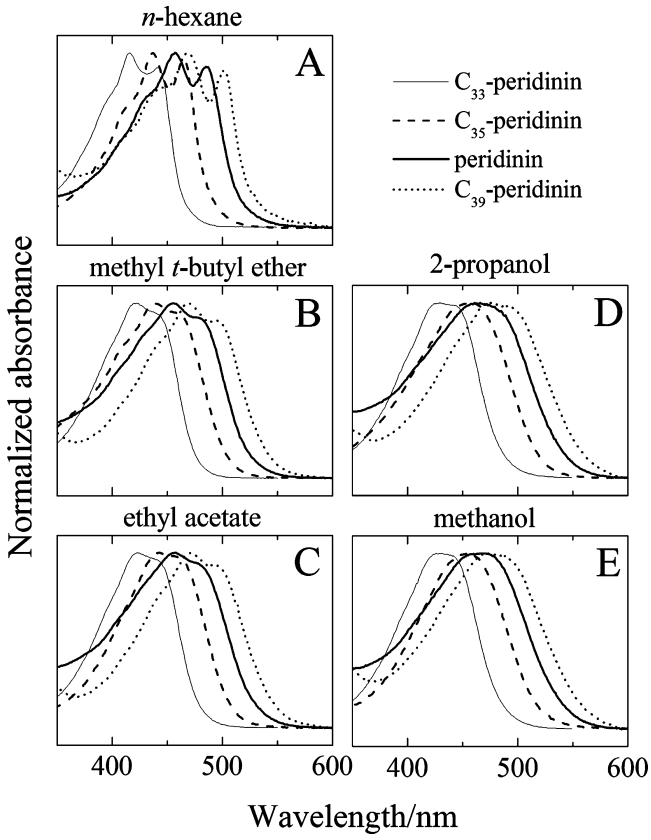

Figure 2. Steady-state absorption spectra of peridinin and synthetic C_{33}-, C_{35}- and C_{39}-peridinin analogues taken in different solvents at room temperature. All spectra were normalized.

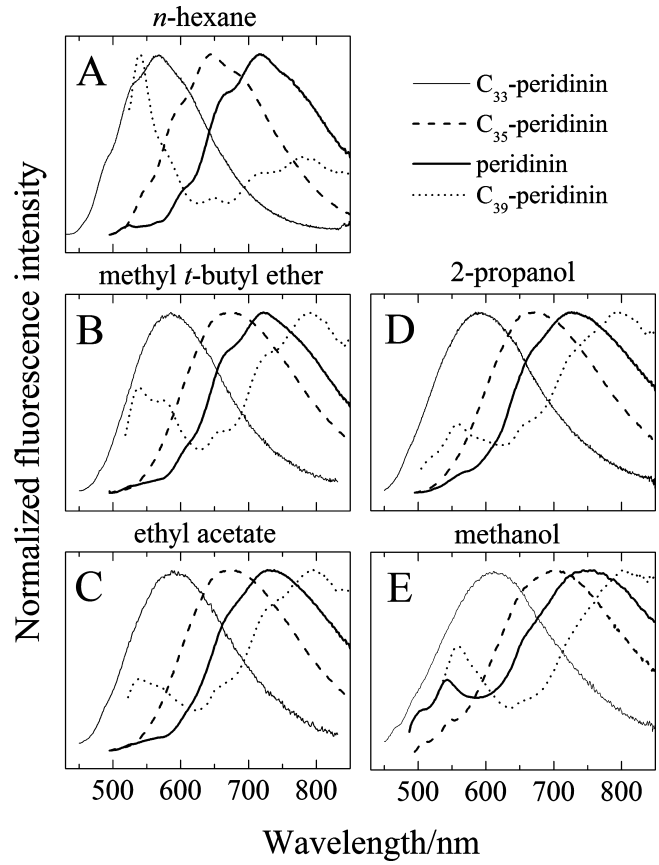

Figure 3. Fluorescence emission spectra of peridinin and synthetic C_{33}-, C_{35}-, and C_{39}-peridinin analogues taken in different solvents at room temperature. All spectra were normalized.

wavelength side of the dip increases in intensity, ultimately resulting in a less broad, symmetric, blue-shifted band; for example, at around 550 nm in ethyl acetate (Figure 4C). The precise wavelength maximum of this remaining band depends on the solvent and shifts to shorter wavelength as the solvent polarity increases. Note that it shifts from ~625 nm in *n*-hexane (green trace in Figure 4A) to ~520 nm in methanol (green trace in Figure 4E).

Excitation of the next molecule in the series, C_{35}-peridinin, in all solvents shows an immediate rise of a long wavelength band at ~700 nm (red traces in Figure 4F−J) that disappears after a few hundred femtoseconds. Subsequently, a broadband between 500 and 700 nm appears (green traces in Figure 4F−J). In *n*-hexane, this broadband exhibits structural features (green trace in Figure 4F). In addition, in *n*-hexane (Figure 4F), a strong band appears at 490 nm. This band decreases in intensity with increasing solvent polarity, but it can be seen in C_{35}-peridinin as a small shoulder in MTBE (Figure 4G), as an inflection in ethyl acetate (Figure 4H) on the short wavelength side of the broadband, and in the longer time (≥10 ps) traces for C_{35}-peridinin in 2-propanol (Figure 4I) and methanol (Figure 4J).

Note that the 1 ps traces for C_{33}-peridinin and C_{35}-peridinin in the polar solvents (green traces in Figure 4B−E and G−J) dip below the baseline in the region 650−800 nm. This is due to a tail of stimulated emission that appears in the NIR region and originates from the ICT state.[8,27] This assignment is supported by transient absorption experiments probed in the NIR region between 800 and 1250 nm (Figure S2), which show pronounced emission extending below 800 nm for all the molecules dissolved in methanol except C_{39}-peridinin.

Transient absorption spectra of the third molecule in the series, peridinin, have been described in several previous publications.[8,9,18,19] Similar to what is observed for C_{35}-peridinin, in all the solvents, there is an immediate rise of a long wavelength band between 700 and 800 nm (black traces in Figure 4K−O) that disappears after a few hundred femtoseconds. Its very short lifetime strongly suggests that this signal is due to an $S_2 \rightarrow S_n$ transition. Subsequently, both a broad, long-wavelength band, and a sharper, short-wavelength band appear (green traces in Figure 4K−O). The intensity of the broad, long-wavelength band increases and shifts to the blue with increasing solvent polarity relative to that of the sharper, short-wavelength band. As will be discussed in more detail below, the short-wavelength band can be attributed to an $S_1 \rightarrow S_n$ transition, and the long-wavelength band is assigned to a transition originating from the ICT state whose energy is stabilized in polar solvents.[9] This accounts for the blue shift of the ICT $\rightarrow S_n$ transition with increasing solvent polarity.

Excitation of the longest molecule in the series, C_{39}-peridinin, results in the rapid build-up of a narrow ESA band at short wavelengths and the appearance of broad ESA features at longer wavelengths (green traces in Figure 4P−T). The longer-wavelength features become more prominent as the polarity of the solvent increases. In the nonpolar solvent, *n*-hexane (Figure 4P), the narrow, short-wavelength band dominates the broad, long-wavelength features, whereas in the polar solvent, methanol (Figure 4T), the two signals have comparable intensity.

Kinetics Analysis. To obtain the excited-state dynamics of the molecules, transient profiles corresponding to the maxima of the $S_1 \rightarrow S_n$ and ICT $\rightarrow S_n$ spectra shown in Figure 4 were fit to a sum of exponentials function. Table 1 summarizes the results of the kinetics analysis. Figure 5 shows the solvent dependence of the decay kinetics of the ESA signals corre-

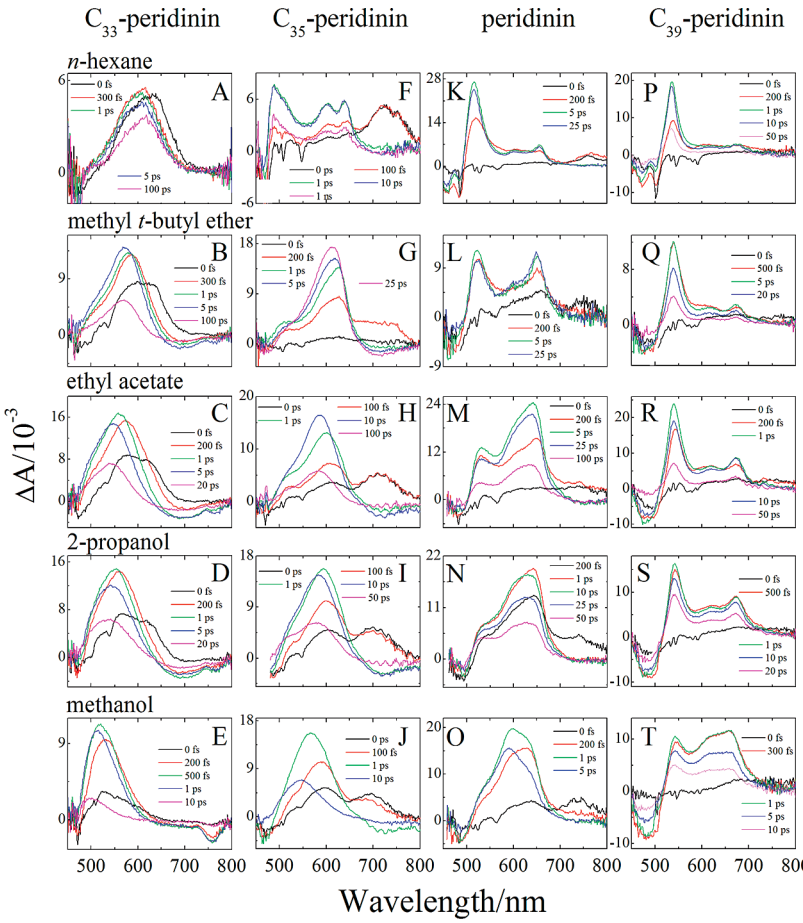

Figure 4. Transient absorption spectra of peridinin and synthetic C_{33}-, C_{35}-, and C_{39}-peridinin analogues taken at different time delays after excitation in different solvents at room temperature.

sponding to the longer wavelength (ICT → S_n) feature in the spectra. The solid lines represent the fits obtained from the kinetics analysis. For C_{33}-peridinin (Figure 5A), there is a short-lived spike at very early times in the traces. This is due to the rapid appearance and decay of the $S_2 \rightarrow S_n$ absorption band in this wavelength region. At longer times, the decay dynamics of C_{33}-peridinin show an extreme sensitivity to solvent polarity. The lifetime of the excited state is slowest in *n*-hexane, and faster by a factor of ~500 in methanol. This is the largest solvent effect on the excited-state lifetime of a carotenoid yet reported. The lifetime of this same component for the other molecules becomes both faster and less sensitive to solvent polarity as the extent of π-electron conjugation increases. (Note the decreasing time values on the horizontal scale of Figure 5A−D.) The data show that the threshold at which the kinetics change with solvent polarity increases with increasing length of the analogue. The lifetime of C_{33}-peridinin (Figure 5A) is 4.2 ns in *n*-hexane and drops to 200 ps upon changing the solvent to MTBE, then ultimately drops by more than an order of magnitude to 10 ps in methanol. In contrast, the lifetime of C_{39}-peridinin (Figure 5D) is a constant 41 ps in *n*-hexane, MTBE, and ethyl acetate, then drops to ~30 ps in 2-propanol, finally reaching 9 ps in methanol. Previous studies on peridinin have shown that below a solvent polarity value, $P(\varepsilon) \approx 0.5$, the lifetime is constant at ~165 ps, whereas above this polarity value, the lifetime decreases linearly with solvent polarity.[10] One additional noteworthy point about these kinetics data is that although the lifetimes of the molecules in the nonpolar solvent, *n*-hexane, are strikingly different, varying from 4.2 ns for C_{33}-peridinin to 41 ps for C_{39}-peridinin in *n*-hexane, the lifetimes of all of the molecules converge to essentially the same value of 10.0 ps (within a range ± 2.0 ps) in the polar solvent, methanol. Previous studies on apo-carotenals and apo-carotenoic acids have shown similar trends and convergences.[12−14]

Figure 6 presents an overlay of the kinetics of the short- ($S_1 \rightarrow S_n$) and long- (ICT → S_n) wavelength ESA signals taken from C_{35}-peridinin, peridinin, and C_{39}-peridinin in methanol. The decay kinetics of the $S_1 \rightarrow S_n$ ESA signals were observed to be slower than those associated with the ICT → S_n signals, which suggests that the S_1 and ICT states not only have distinct spectral profiles but also deactivate independently of one another. The values of the kinetic parameters are summarized in Table 1.

Fluorescence Kinetics. Due to the fact that the lifetime of the lowest excited singlet state of C_{33}-peridinin and C_{35}-peridinin in *n*-hexane is either comparable to or exceeds the long-time resolution limit of the transient laser spectrometer, the values were also measured using TCSPC fluorescence methods. The results are shown in Figure 7. The strong emission bands from the S_1 states of these molecules in *n*-hexane (Figure 3A) facilitated the detection of the fluorescence transient decay signals. The signals were monitored in the (0−0) vibronic bands at 490 nm for C_{33}-peridinin and at 550 nm for C_{35}-peridinin of their S_1 steady-state fluorescence spectra (Figure 3A). The lifetimes obtained from fitting the data to a single exponential decay function were 4.2 ± 0.2 ns for C_{33}-peridinin and 1.0 ± 0.1 ns for C_{35}-peridinin.

Discussion

Steady-State Absorption and Fluorescence. In addition to a red shift in their absorption spectra with increasing π-electron

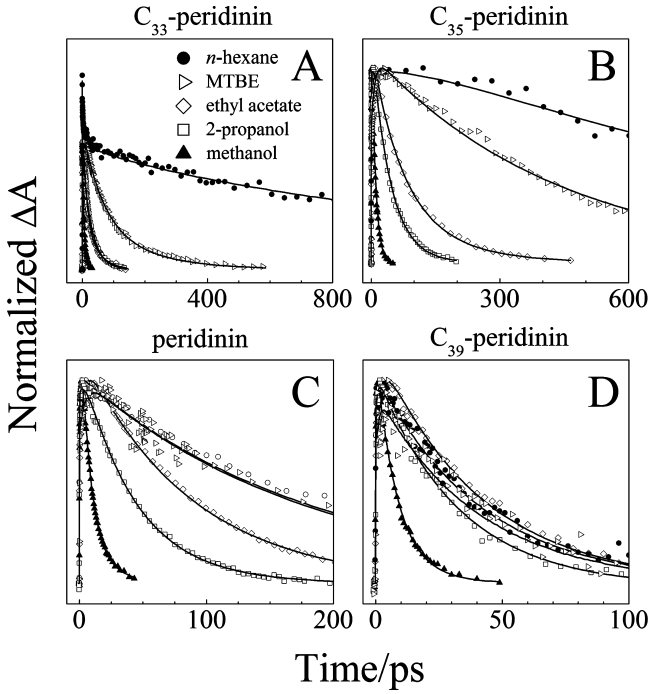

Figure 5. Representative kinetic traces (symbols) with fits obtained at single wavelengths (lines) in the long wavelength range of the transient absorption spectra. For C_{33}-peridinin, the kinetics were probed at 620 (*n*-hexane), 567 (MTBE), 551 (ethyl acetate), 533 (2-propanol), and 518 nm (methanol). For C_{35}-peridinin, the probe wavelengths were 640 (*n*-hexane), 610 (MTBE), 586 (ethyl acetate), 587 (2-propanol), and 560 nm (methanol). For peridinin, the probe wavelengths were 654 (*n*-hexane), 649 (MTBE), 639 (ethyl acetate), 639 (2-propanol), and 590 nm (methanol). For C_{39}-peridinin, the probe wavelengths were 672 (*n*-hexane), 684 (MTBE), 674 (ethyl acetate), 671 (2-propanol), and 649 nm (methanol). All kinetics traces were normalized for clarity.

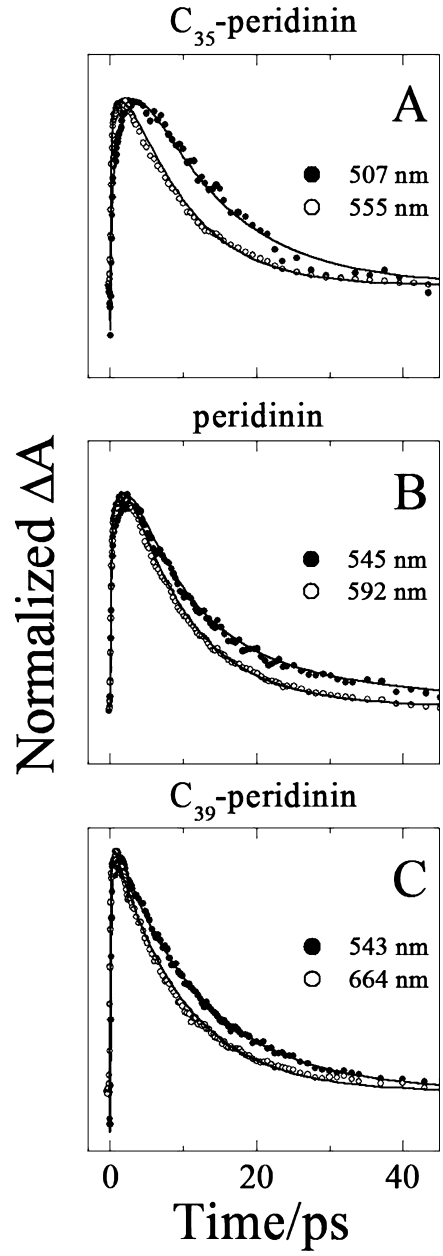

Figure 6. Overlay of the kinetics probed at the maxima of the short- ($S_1 \rightarrow S_n$) and long- (ICT $\rightarrow S_n$) wavelength ESA signals taken from (A) C_{35}-peridinin, (B) peridinin, and (C) C_{39}-peridinin in methanol at room temperature.

conjugation, the series of peridinin analogues studied here exhibit substantial line-broadening and loss of vibronic resolution when the molecules are dissolved in increasingly polar solvents (Figure 2). This behavior is typical of carotenoids possessing a carbonyl group in conjugation with the π-electron system of carbon−carbon double bonds and can be attributed to an increase in the number of conformational isomers formed when the molecules are dissolved in polar solvents. Each of the conformational isomers will have a slightly different absorption spectrum so that the ensemble average results in a broad line shape.[22,28] Enhanced spectral broadening and the loss of vibronic features with increasing solvent polarity are also observed in the $S_1 \rightarrow S_0$ fluorescence spectra of the molecules (Figure 3). This can also be accounted for on the basis of enhanced conformational disorder of the molecules in the polar solvents.

With the exception of C_{39}-peridinin, the emission spectra of all the molecules in all solvents are dominated by S_1-like fluorescence (Figure 3) which is typical of short ($N \leq 8$) carotenoids. Dominant S_1 emission occurs due to a small $S_2 - S_1$ energy gap that promotes nonradiative internal conversion from S_2 leading to a diminished yield of fluorescence from the S_2 state.[5,29] For longer carotenoids ($N \geq 10$) that have larger $S_2 - S_1$ energy gaps, the rate of $S_2 \rightarrow S_1$ internal conversion is decreased, and this enhances the probability of S_2 emission. C_{39}-peridinin behaves like an intermediate-length ($10 \geq N \geq 8$) carotenoid and displays dual S_1 and S_2 state emission in all solvents (Figure 3A−E). Dual emission is typically seen in moderately long carotenoids and is due to the fact that with increasing π-electron chain length, the energy gap between S_2 and S_1 increases, which slows the rate of nonradiative decay from S_2 to the point that excited state deactivation by radiative means becomes competitive with $S_2 \rightarrow S_1$ internal conversion. However, C_{39}-peridinin is unique in that the yield of emission from S_2 relative to S_1 changes dramatically with the polarity of the solvent (dotted lines in Figure 3). C_{39}-peridinin has a higher amplitude of S_2 emission in the nonpolar solvent, *n*-hexane. In more polar solvents, the S_1-like emission dominates. This indicates that the rate of internal conversion from S_2 increases with solvent polarity, leading to a reduced emission yield relative to that of S_1. The small dependence on solvent polarity of the energies of the S_1 and S_2 states is not sufficient to account for this distinctive effect. Most likely, the observation can be traced to the solvent-induced modulation of the energy of the ICT state near S_1 and S_2 because the energy of the ICT state does depend strongly on solvent polarity. A diminished yield of S_2 fluores-

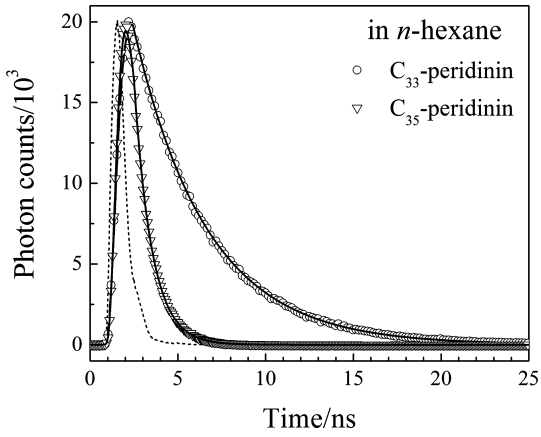

Figure 7. Kinetics of the S_1 state fluorescence decay of C_{33}-peridinin and C_{35}-peridinin. The experimental traces (symbols) were recorded at room temperature at 490 nm for C_{33}-peridinin and at 550 nm for C_{35}-peridinin. The solid lines represent monoexponential fits to the experimental data sets. The short-lived dashed trace shows the instrument response function.

cence from C_{33}-peridinin with increasing solvent polarity will be seen if the rate of populating the ICT state from S_2 also increases with solvent polarity. This may seem counterintuitive since the energy gap between S_2 and the ICT state is likely to become larger as the ICT state is stabilized with increasing solvent polarity. However, the effect can be rationalized if the controlling factor in depopulating S_2 via the ICT state is not the magnitude of the energy gap between these states, but rather, the size of the apparent activation barrier at the crossing point between the S_2 and ICT potential energy surfaces. In this case, increasing solvent polarity would stabilize the ICT state, lower the apparent activation barrier for population transfer from S_2 to the ICT state, and lead to faster nonradiative decay from S_2, which would diminish the relative yield of S_2 emission, as observed.

The Kinetics of the S_1 State. The kinetics of the S_1 state for these molecules have been obtained using TCSPC techniques (for C_{33}-peridinin and C_{35}-peridinin) and single-wavelength analyses of the transient absorption data. In a given solvent, the S_1 lifetime of the molecules was found to decrease with increasing N. For example, in *n*-hexane, the S_1 lifetime for the series of molecules decreased from 4.2 ns to 41 ps in going from C_{33}-peridinin to C_{39}-peridinin. This is attributable to the fact that the S_1 energy decreases with increasing N. It has been demonstrated for carotenoids[30] that the rate of internal conversion increases exponentially with decreasing energy gap between the S_1 and S_0 states in accordance with the energy gap law for radiationless transitions.[31] In addition, the present data show clearly that the shorter the peridinin analogue, the stronger the effect of polarity on the excited-state lifetime. This effect is central to the question of the origin of the ICT state whose properties can be explained by a consideration of its position relative to the energies of the S_1 and S_2 states.

The Nature of the ICT State. The most striking observation in the kinetics data is that the lifetime of the ICT state is essentially the same (10.0 ± 2.0 ps) for all four molecules examined in the polar solvent, methanol. This convergence to a common value for these four molecules, which differ in their extents of π-electron conjugation, indicates that the ICT state must be localized away from the extended π-electron chain and on or near the lactone-ring, which remains a constant structural component for all of the molecules. The obligatory requirement of the carbonyl group for inducing the effect of solvent on the excited-state lifetime of carotenoids has been demonstrated previously[9,10] and also has been reported for apo-carotenals and apo-carotenoic acids.[12−14] The lack of sensitivity to the extent of the π-electron conjugation seen in these series of molecules not only suggests that the ICT state is highly localized but also argues that the ICT state decays independently from the S_1 state, whose energy changes by ~2000 cm^{-1} with each incremental change in *N*. This idea is supported by the observation that the $S_1 \rightarrow S_n$ and ICT $\rightarrow S_n$ transitions display different spectra (Figure 4) and decay kinetics (Figure 6, Table 1). However, it cannot be stated for certain whether these differences result from the S_1 and ICT states being uncoupled or from a situation in which the two states are strongly coupled and correspond to different minima on the same potential energy surface.

The trends observed in the spectral features and dynamics for this series of molecules can be accounted for on the basis of changes in the relative energies of the S_1, S_2, and ICT excited states with changing *N* and solvent polarity. As the π-electron conjugation chain length of the molecules increases, both the S_1 and S_2 states decrease in energy. As the polarity of the solvent increases from *n*-hexane to methanol, the ICT state is stabilized. Thus, changes in chain length and solvent polarity can lead to differences in the population of the S_1 and ICT states evidenced by the appearance of different ESA signal intensities associated with transitions from these states (Figure 4).

From the ESA traces presented for all four molecules and shown in Figure 4, it is clear that C_{39}-peridinin in methanol (blue trace in Figure 4T), peridinin in MTBE (blue trace Figure 4L), and C_{35}-peridinin in *n*-hexane (red trace in Figure 4F) have very similar line shapes in that they show comparable amplitudes associated with the $S_1 \rightarrow S_n$ and ICT $\rightarrow S_n$ transitions. For all other molecule/solvent pairings displayed in Figure 4, features associated with one or the other of these transitions dominates the profiles, suggesting that either the S_1 state or the ICT state is lower in energy than the other. Under conditions that the ICT state lies below the S_1 state, the $S_1 \rightarrow S_n$ spectrum is broadened and the lifetime of the S_1 state is shortened (Table 1) due to transfer of population from S_1 to the ICT state. Under conditions that the ICT state lies above S_1, little if any effect on the $S_1 \rightarrow S_n$ spectrum and S_1 lifetime is seen.

Therefore, it is proposed that for the three special molecule/solvent pairs, C_{39}-peridinin in methanol (blue trace in Figure 4T), peridinin in MTBE (blue trace Figure 4L), and C_{35}-peridinin in *n*-hexane (blue trace in Figure 4F), the ICT and S_1 state energies are very close in energy. Because the S_1 energies of the molecules can be determined from the spectral origins of the $S_1 \rightarrow S_0$ fluorescence spectra (Figure 3), the ICT state energies of the three molecules in these solvents are then simultaneously determined. A plot of these three values versus solvent polarity (open circles in Figure 8) yields a precisely straight line along which the entire range of energy values for the ICT states of all four molecules in all solvents, including MTBE and 2-propanol (filled circles in Figure 8), can be determined. The plot shows that the highest energy the ICT state can achieve is 18 300 cm^{-1} in the nonpolar solvent, *n*-hexane. The minimum energy of the ICT state is 15 150 cm^{-1} in the polar solvent, methanol. A plot of the energies of the S_1 and S_2 states of the four molecules determined from their steady-state absorption (Figure 2) and fluorescence (Figure 3) spectra shows that the S_1 and S_2 state energies follow a linear dependence according to the function $1/(1 \pm 2N)$ (Figure 9). Moreover, the S_1 state energy decreases more rapidly with increasing *N* than does the S_2 state energy.

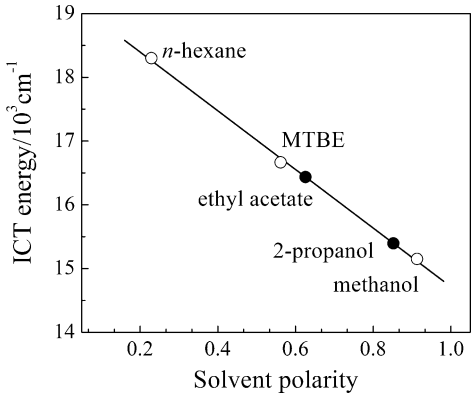

Figure 8. Plot of the ICT state energies as a function of solvent polarity in *n*-hexane (0.229, 18,300 cm^{-1}), MTBE (0.562, 16,670 cm^{-1}), and methanol (0.913, 15,150 cm^{-1}) (open circles). The ICT state energy values in ethyl acetate (0.626, 16,440 cm^{-1}) and 2-propanol (0.852, 15,400 cm^{-1}) (solid circles) were assumed from the linear fit.

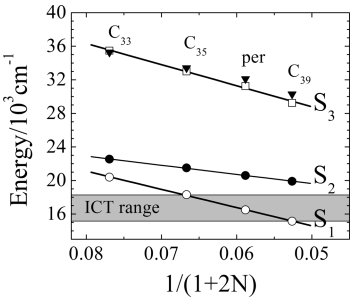

Figure 9. Overlay of the S_2 state (solid circles) and S_1 state (open circles) energies with the range of possible ICT state energies (shaded region) as a function of $1/(1 \pm 2N)$ where N is the number of conjugated carbon−carbon double bonds assumed to vary from $N = 6$ for C_{33}-peridinin to $N = 9$ for C_{39}-peridinin. The S_2 state energies were obtained from steady-state absorption in *n*-hexane ((0−0) vibronic bands). The S_1 state energies were obtained from steady-state fluorescence in *n*-hexane. The S_3 state energies (open squares) were obtained from the positions of the cis peaks in the steady-state absorption spectra in methanol ((0−0) vibronic bands) (Figure S3) fit to a straight line. The filled triangles indicate the sum of the energy of the ICT state in methanol (15 150 cm^{-1}) and the energy of the ICT → S_n transition observed in the excited state absorption spectra taken in methanol (Figure 4E, J, O, and T).

Comparing the range of possible ICT state energies (obtained from Figure 8 and represented by the shaded region in Figure 9) with the energies of the S_1 and S_2 states shows clearly that for the shortest molecule in the series, C_{33}-peridinin, the ICT state energy is always lower than the S_1 state energy of this molecule, regardless of solvent polarity. At the other extreme, for the longest molecule examined here, C_{39}-peridinin, the ICT state energy lies above its S_1 state energy for all solvents except the most polar solvent, methanol, in which the two states are isoenergetic. For C_{35}-peridinin, the S_1/ICT energy equivalence point is achieved when the molecule is dissolved in the nonpolar solvent, *n*-hexane. For peridinin, the ICT and S_1 states will have roughly equivalent energies in solvents having a polarity index midway between *n*-hexane and methanol.

Figure 9 also shows S_3 state energies (open squares) obtained from the positions of the cis peaks in the steady-state absorption spectra in methanol (Figure S3) fit to a straight line. Cis peaks corresponding to $S_0 \rightarrow S_3$ transitions are readily observed in the spectra of *cis*-carotenoids due to less stringent selection rules for light absorption for molecules having undergone trans-to-cis isomerization.[32,33] The solid triangles in Figure 9 indicate the sum of the energy of the ICT state in methanol (15 150 cm^{-1}) and the energy of the ICT → S_n transition observed in the excited-state absorption spectra also taken in methanol (Figure 4E, J, O, and T). The fact that these two sets of points (open squares and solid triangles) are in such good agreement indicates that the end state of the ICT → S_n transition is S_3. The strong allowedness of the ICT → S_n (S_3) transition (Figure 4) can then be thought of as deriving from asymmetry in the wave function of the ICT state that relaxes the selection rules for light absorption between the ICT and S_3 states, analogous to what occurs for the $S_0 \rightarrow S_3$ transition.

This analysis provides an explanation why C_{33}-perinidin shows only very little evidence in its transient absorption spectra (Figure 4A−E) of transitions associated with the S_1 state. The ICT state in C_{33}-peridinin is so low in energy in all solvents that not only is it rapidly populated directly from the S_2 state after photoexcitation, but it also depopulates the S_1 state very rapidly. The ESA spectra obtained are shown in Figure 4A−E and are consistent with this conclusion. The data indicate that the very short-lived $S_2 \rightarrow S_n$ transition appears simultaneously with the ICT → S_n transition, showing that the ICT state is populated within the time of the laser excitation pulse. After the S_2 state decays in <170 fs, the ICT state remains, but the rapid population of the ICT state has left it vibronically hot, as evidenced by the fact that after ~1 ps, depending on the solvent, the ICT → S_n transition narrows and blue-shifts (red and blue traces in Figure 4A−E). The remaining, vibronically relaxed ICT → S_n band (blue traces in Figure 4A−E) persists for a time ranging from >1 ns in the nonpolar solvent, *n*-hexane, to 10 ps in the polar solvent, methanol. In *n*-hexane, MTBE and ethyl acetate, an additional minor decay component is required to achieve a satisfactory fit to the data sets for C_{33}-peridinin. The origin of this component remains unclear at this time, and it was not needed for a good fit to the kinetic data from the other molecules.

Like C_{33}-peridinin, the S_2 state of C_{39}-peridinin decays directly into both the S_1 and the ICT states in <170 fs. This is clear from the rapid rise of ESA associated with both states. In nonpolar solvents, there occurs a slight narrowing and blue-shifting of the resulting $S_1 \rightarrow S_n$ and ICT → S_n transitions that can be attributed to vibronic cooling. As the solvent polarity increases (Figure 4P-T), features associated with the ICT state are seen, and in methanol (Figure 4T), this kinetic component decays in 9 ps (Table 1). Similar conclusions regarding the kinetic behavior of C_{35}-peridinin and peridinin can be drawn. For these two molecules, it is clear from the ESA traces presented in Figure 4F−O and the data in Table 1 that in most cases, the S_2 state decays in <170 fs and directly populates both the S_1 and the ICT states. Subsequently, ESA profiles associated with either the $S_1 \rightarrow S_n$ or ICT → S_n transitions are seen, depending on the relative energy ordering of the states.

The energies of the transitions and the apparent activation barriers for the transfer of population between the states are summarized in a series of potential energy surface diagrams given in Figure 10. The figure is drawn as if the states are quantum-mechanically uncoupled, but the data presented here do not distinguish between this possibility and the alternative that the states are strongly coupled and represent different minima on the same potential energy surface. For C_{33}-peridinin in both nonpolar and polar solvents, the apparent activation barrier for the transfer of population from S_1 to the ICT state is likely to be very small. This would explain why there is little evidence in the transient absorption spectra (Figure 4A−E) of features associated with an $S_1 \rightarrow S_n$ transition. At the other extreme, for C_{39}-peridinin, efficient transfer of population from

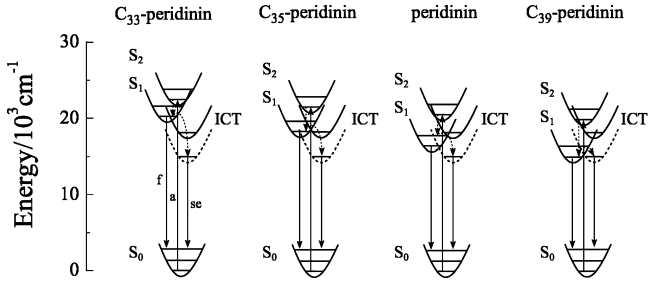

Figure 10. Potential energy level diagrams and associated spectroscopic transitions for the molecules in polar and nonpolar solvents: f, fluorescence; a, absorption; se, stimulated emission. The solid lines correspond to radiative transitions, and the dashed lines correspond to nonradiative processes. The potential energy surface for the ICT state shown as a solid line represents its position in the nonpolar solvent, *n*-hexane. The potential energy surface for the ICT state shown as a dashed line represents its position in the polar solvent, methanol.

S_1 to the ICT state occurs only when the molecule is dissolved in highly polar solvents and when the two states are close in energy.

Conclusions

In the present work, steady-state and ultrafast time-resolved optical spectroscopy have been performed on peridinin and three synthetic analogues, C_{33}-peridinin, C_{35}-peridinin, and C_{39}-peridinin, which differ in their extents of π-electron conjugation. The trends in the positions of the steady-state and transient spectral profiles for this systematic series of molecules have allowed an assignment of the spectral features to transitions involving the various excited electronic singlet states, including the ICT state. A kinetics analysis revealed that the dependence on solvent polarity of the excited state lifetime gets stronger as the extent of π-electron conjugation of the carotenoid is reduced. However, the most striking observation in these data is that the lifetime of the ICT state converges to the same value of 10.0 ± 2.0 ps in the polar solvent, methanol, for all the peridinin analogues regardless of the extent of π-electron conjugation. This suggests that the ICT state is localized on the lactone ring, which is the common, carbonyl-containing, structural feature in all four molecules. In addition, the kinetics data are best explained assuming the S_1 and ICT states deactivate independently, the rate of which is found here to depend strongly on both solvent polarity and the extent of π-electron conjugation of the carotenoid.

Acknowledgment. The authors thank Professors Robert Birge and Tomáš Polívka for many useful discussions. This work has been supported in the laboratory of H.A.F. by grants from the National Institutes of Health (GM-30353), the National Science Foundation, and the University of Connecticut Research Foundation. We also thank Dr. Thomas Netscher of DSM Nutritional Products, Ltd., for the donation of (−)-actinol. This work has been supported in the laboratory of S.K. by a Grant-in-Aid for Science Research on Priority Areas 16073222 from the Ministry of Education, Culture, Sports, Science and Technology, and Matching Fund Subsidy for a Private University, Japan.

Supporting Information Available: Overlay of the fluorescence spectra of C_{33}-peridinin, C_{35}-peridinin, and peridinin taken at room temperature in carbon disulfide and *n*-hexane, NIR transient spectra of all four analogues taken at room temperature in methanol, and steady-state absorption spectra of C_{33}-peridinin, C_{35}-peridinin, peridinin, and C_{39}-peridinin taken at room temperature in methanol, extended to high energy to show the "cis peak" region between 27 000 and 40 000 cm^{-1}. This material is available free of charge via the Internet at http://pubs.acs.org.

References and Notes

(1) Pariser, R. *J. Chem. Phys.* **1955**, *24*, 250.
(2) Hudson, B.; Kohler, B. *Annu. Rev. Phys. Chem.* **1974**, *25*, 437.
(3) Callis, P. R.; Scott, T. W.; Albrecht, A. C. *J. Chem. Phys.* **1983**, *78*, 16.
(4) Birge, R. R. *Acc. Chem. Res.* **1986**, *19*, 138.
(5) Christensen, R. L.; Barney, E. A.; Broene, R. D.; Galinato, M. G. I.; Frank, H. A. *Arch. Biochem. Biophys.* **2004**, *430*, 30.
(6) Hudson, B. S.; Kohler, B. E. *J. Chem. Phys.* **1973**, *59*, 4984.
(7) Hudson, B. S.; Kohler, B. E.; Schulten, K. Linear polyene electronic structure and potential surfaces. *In Excited States*; Lim, E. D., Ed.; Academic Press: New York, 1982; Vol. 6; pp 1.
(8) Polívka, T.; Sundström, V. *Chem. Rev.* **2004**, *104*, 2021.
(9) Bautista, J. A.; Connors, R. E.; Raju, B. B.; Hiller, R. G.; Sharples, F. P.; Gosztola, D.; Wasielewski, M. R.; Frank, H. A. *J. Phys. Chem. B* **1999**, *103*, 8751.
(10) Frank, H. A.; Bautista, J. A.; Josue, J.; Pendon, Z.; Hiller, R. G.; Sharples, F. P.; Gosztola, D.; Wasielewski, M. R. *J. Phys. Chem. B* **2000**, *104*, 4569.
(11) Wild, D. A.; Winkler, K.; Stalke, S.; Oum, K.; Lenzer, T. *Phys. Chem. Chem. Phys.* **2006**, *8*, 2499.
(12) Ehlers, F.; Wild, D. A.; Lenzer, T.; Oum, K. *J. Phys. Chem. A* **2007**, *111*, 2257.
(13) Kopczynski, M.; Ehlers, F.; Lenzer, T.; Oum, K. *J. Phys. Chem. A* **2007**, *111*, 5370.
(14) Stalke, S.; Wild, D. A.; Lenzer, T.; Kopczynski, M.; Lohse, P. W.; Oum, K. *Phys. Chem. Chem. Phys.* **2008**, *10*, 2180.
(15) Chatterjee, N.; Niedzwiedzki, D. M.; Kajikawa, T.; Hasegawa, S.; Katsumura, S.; Frank, H. A. *Chem. Phys. Lett.* **2008**, *463*, 219.
(16) Vaswani, H. M.; Hsu, C. P.; Head-Gordon, M.; Fleming, G. R. *J. Phys. Chem. B* **2003**, *107*, 7940.
(17) Papagiannakis, E.; Larsen, D. S.; van Stokkum, I. H. M.; Vengris, M.; Hiller, R. G.; van Grondelle, R. *Biochem.* **2004**, *43*, 15303.
(18) Papagiannakis, E.; Vengris, M.; Larsen, D. S.; van Stokkum, I. H. M.; Hiller, R. G.; van Grondelle, R. *J. Chem. Phys. B* **2006**, *110*, 512.
(19) Van Tassle, A. J.; Prantil, M. A.; Hiller, R. G.; Fleming, G. R. *Isr. J. Chem.* **2007**, *47*, 17.
(20) Zigmantas, D.; Hiller, R. G.; Yartsev, A.; Sundström, V.; Polivka, T. *J. Phys. Chem. B* **2003**, *107*, 5339.
(21) Linden, P. A.; Zimmermann, J.; Brixner, T.; Holt, N. E.; Vaswani, H. M.; Hiller, R. G.; Fleming, G. R. *J. Chem. Phys. B* **2004**, *108*, 10340.
(22) Shima, S.; Ilagan, R. P.; Gillespie, N.; Sommer, B. J.; Hiller, R. G.; Sharples, F. P.; Frank, H. A.; Birge, R. R. *J. Phys. Chem. A* **2003**, *107*, 8052.
(23) Martinson, T. A.; Plumley, G. F. *Anal. Biochem.* **1995**, *228*, 123.
(24) Bautista, J. A.; Hiller, R. G.; Sharples, F. P.; Gosztola, D.; Wasielewski, M.; Frank, H. A. *J. Phys. Chem. A* **1999**, *103*, 2267.
(25) Ilagan, R. P.; Koscielecki, J. F.; Hiller, R. G.; Sharples, F. P.; Gibson, G. N.; Birge, R. R.; Frank, H. A. *Biochemistry* **2006**, *45*, 14052.
(26) Ziólek, M.; Lorenc, M.; Naskrecki, R. *Appl. Phys. B: Laser Opt.* **2001**, *72*, 843.
(27) Zigmantas, D.; Polivka, T.; Hiller, R. G.; Yartsev, A.; Sundström, V. *J. Phys. Chem. A* **2001**, *105*, 10296.
(28) Christensen, R. L.; Kohler, B. E. *Photochem. Photobiol.* **1973**, *18*, 293.
(29) Christensen, R. L.; Galinato, M. G. I.; Chu, E. F.; Fujii, R.; Hashimoto, H.; Frank, H. A. *J. Am. Chem. Soc.* **2007**, *129*, 1769.
(30) Chynwat, V.; Frank, H. A. *Chem. Phys.* **1995**, *194*, 237.
(31) Englman, R.; Jortner, J. *Mol. Phys.* **1970**, *18*, 145.
(32) Isler, O. *Carotenoids*; Birkhauser: Basel, 1971.
(33) Niedzwiedzki, D. M.; Sandberg, D. J.; Cong, H.; Sandberg, M. N.; Gibson, G. N.; Birge, R. R.; Frank, H. A. *Chem. Phys.* **2008**, *357*, 4.

JP903923R